Chapter 5

Differential Cross-sections for Ar-Ar+

Laser-induced fluorescence measurements in low pressure ECR reactors (Sadeghi *et al* (1991), den Hartog *et al* (1990)) have found that argon ion temperatures perpendicular to the applied electric field can be 10 times greater than that of the neutral gas temperature within the bulk. Hence ion collisions with the background gas atoms must be involved in transferring energy obtained by the ions through acceleration in the field, to directions perpendicular to the field. However, experimental measurements (Vestal *et al* (1978)) show that for ion energies greater than ~1 eV the differential cross-section for ion collisions with atoms is highly anisotropic – having scattering angles close to 0° or 180° in the centre-of-mass frame – which should result in negligible perpendicular heating. This seems to indicate that there is some feature in the cross-sections, at least for low energies, which has a large effect on the ion trajectories but is not well understood.

In manufacturing of micro-electronic devices it is desirable to have control of the angular distribution of the ions at the surface to ensure vertical etching of the substrate. It is therefore necessary to have a detailed understanding of how the ion trajectories are effected by collisions, both within the bulk and in the sheath, and their consequential effect on the angular distribution at the substrate. To understand therefore how ion-neutral collisions modify the ion velocity distribution, the effect of finite scattering angles is investigated by developing a highly accurate model of these collisions. The interaction potentials for Ar-Ar^+ were represented by using a Morse curve fit, and classical techniques used to determine the scattering angle as a function of energy and impact parameter. The details of the derivation are presented in Section 5.1. In Section 5.2 the collision model was used in a one-dimensional Monte Carlo code to determine the differential cross-sections, which were compared to the experimental measurements given in Vestal *et al* . This code simulates argon ions travelling through a background of neutral argon gas allowing determination of the energy division between the parallel and perpendicular directions. Simulation results for drift velocities of ions in constant fields and pressures are compared to theoretical and experimental results in Section 5.3.

5.1 Theory

5.1.1 Fitting the interaction potential

The post-collision trajectories of two colliding particles are determined by their interaction potential. By fitting a curve to the potential, it can be used in a classical calculation to determine the scattering angle of the particles in the centre-of-mass frame. In order to accurately determine the ion scattering as a function of the particle energy and the impact parameter it is important to correctly reproduce the width, c, depth, ε, and position of the potential minimum, r_w.

The potential was fitted using a Morse curve, which consists of two exponentials fitted with results from spectroscopic measurements. This method of representing the interaction potential was originally developed by P.M. Morse in 1929 (Varshni (1957)) for spectroscopic work and accurately models the short range repulsive forces and the potential well, which is important in determining the large scattering angle component of the cross-section. The curve is fitted with theoretical parameters obtained from Lorents *et al* (1973).

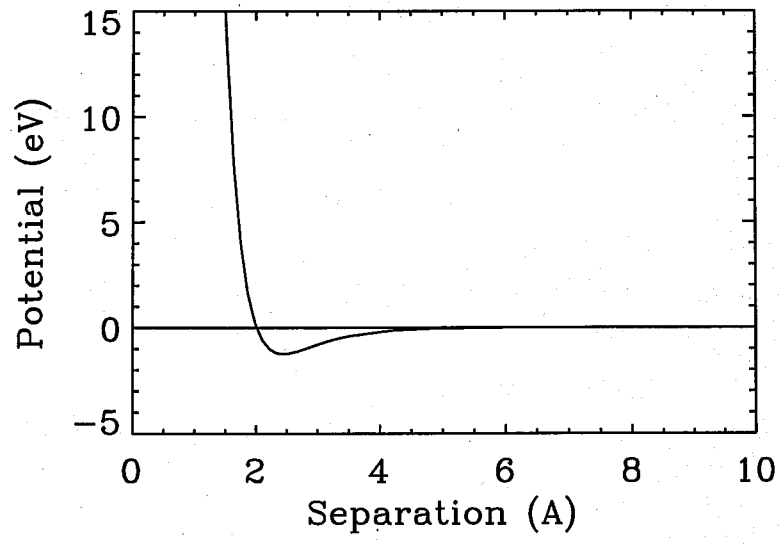

Figure 5.1 The interaction potential for argon, represented using the Morse form given in equation (5.1).

$$V(r) = \varepsilon\left(e^{2cr_w x} - 2e^{cr_w x}\right), \qquad (5.1)$$

where $x = 1 - \frac{r}{r_w}$

r_w = the position of the potential well = 2.438 Å

ε = well depth = 1.25 eV

c = parameter controlling well width = $1.623 \times 10^{10}\ m^{-1}$

5.1.2 *Calculating the Scattering Angle*

Once the potential has been determined the scattering angle can be calculated classically using conservation of energy and momentum. In order to simplify the calculations the two-body scattering problem is reduced to a single reduced mass "virtual" particle scattering about a stationary centre by converting to the centre-of-mass reference frame. This single-body scattering problem is represented schematically in Figure 5.2.

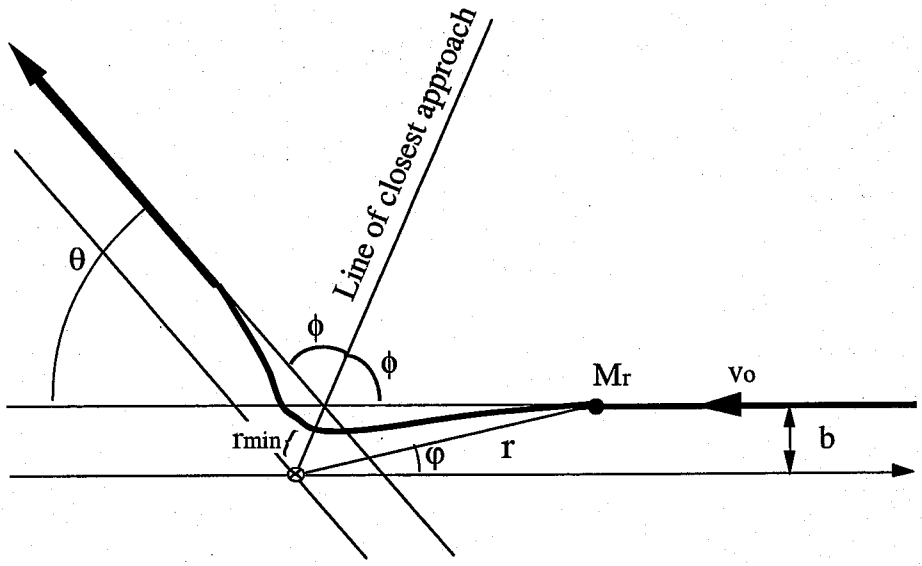

Figure 5.2 Diagram of a reduced mass particle scattering about a point in the centre-of-mass frame. M_r is the reduced particle mass, v_o is its initial velocity, and $\varphi(r)$ the instantaneous angle between the particle and the scattering centre; b is the impact parameter, θ is the scattering angle, r_{min} the distance of closest approach and ϕ the angle at this distance.

In the centre-of-mass frame ϕ, the angle the virtual particle makes with the scattering centre at the distance of closest approach, is given by

$$\phi = -\int_{\infty}^{r_{min}} \frac{d\varphi}{dr}\, dr \quad , \tag{5.2}$$

where φ = instantaneous angle of virtual particle with scattering centre. From conservation of energy and momentum the rate of change of φ with particle separation, r, can be obtained from

$$\frac{d\varphi}{dr} = \frac{\frac{b}{r}}{\sqrt{1 - \frac{V(r)}{\varepsilon_o} - \left(\frac{b}{r}\right)^2}} \quad , \tag{5.3}$$

where ε_O = relative centre-of-mass energy of the particle = $\frac{1}{2}M_r u_o^2$, M_r is the mass of the virtual particle = $\frac{M_{Ar}}{2}$, u_o is the initial velocity of the particle and b is the impact parameter. Substituting (5.3) into (5.2)

$$\phi(\varepsilon_o, b) = -\int_{\infty}^{r_{min}} \frac{\frac{b}{r}}{\sqrt{1 - \frac{V(r)}{\varepsilon_o} - \left(\frac{b}{r}\right)^2}} \quad . \tag{5.4}$$

From symmetry in the centre-of-mass frame, $\theta = \pi - 2\phi$, and so the scattering angle, θ, is given by

$$\theta(\varepsilon_o, b) = \pi - 2\int_{r_{min}}^{\infty} \frac{\frac{b}{r}}{\sqrt{1 - \frac{V(r)}{\varepsilon_o} - \left(\frac{b}{r}\right)^2}}\, dr \quad . \tag{5.5}$$

Note that when $b = 0$ the ion is reflected, since the scattering angle $\theta(\varepsilon_o, b) = \pi$.

The distance of closest approach, r_{min}, is determined from the largest real root of the equation

$$1 - \frac{V(r_{min})}{\varepsilon_o} - \frac{b^2}{r_{min}^2} = 0 \quad . \tag{5.6}$$

If r_{min} is real and non-zero then (5.5) is integrable.

The distance of closest approach, r_{min}, is shown in Figure 5.3 for energies of 0.001, 0.2, 1.0, 10.0, and 500.0 eV. The behaviour of r_{min} can be divided into two different regions. At large impact parameters the potential $V \approx 0$ for all energies, so from equation (5.6) $r_{min} \approx b$. For impact parameters in the range 3 - 9 Å, which corresponds to the region of the potential well, the behaviour of r_{min} is highly dependent on the energy, ε_o. At very small impact parameters the distance of closest approach will be equal to the distance, r, corresponding to the maximum potential

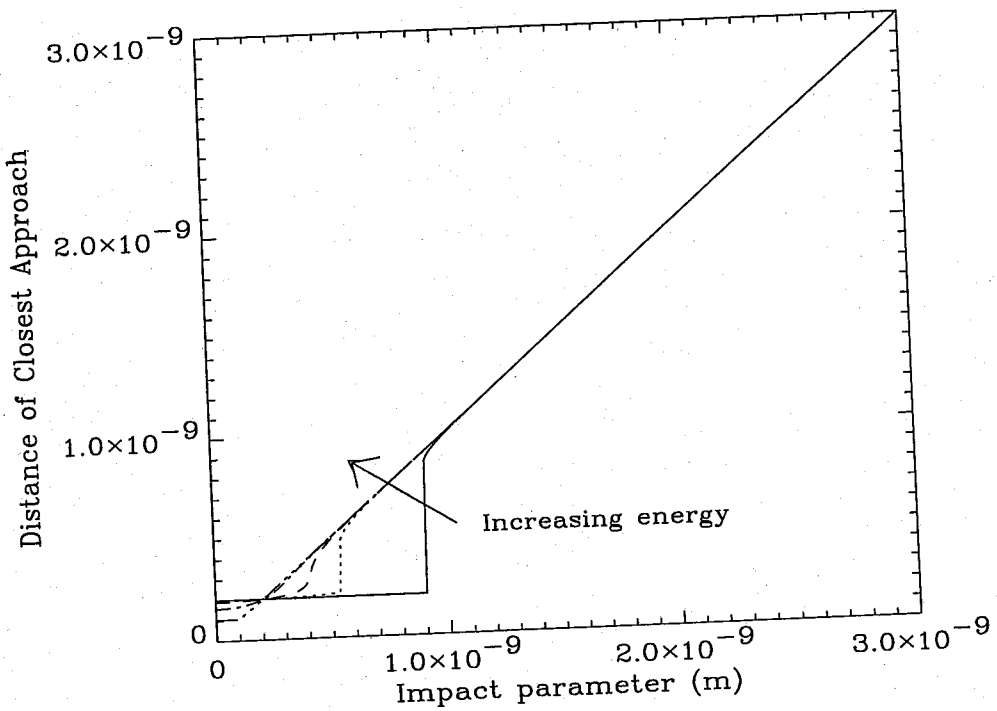

Figure 5.3 Distance of closest approach, r_{min}, as a function of impact parameter for energies 0.001 eV (solid line), 0.2 eV (dotted), 1.0 eV (dashed), 10.0 eV (dash-dot) , 500.0 eV (dash-three dots).

barrier, $V(r) = \varepsilon_o$, that the ion can climb. Ions with small energies can be trapped by the well at large impact parameters, and will therefore attain values of $r_{min} \approx 2$ Å (the

distance at which the potential becomes positive) before being scattered. Ions with energies larger than the well depth of 1.25 eV will be less effected by the well and will be reflected from the potential barrier at much smaller impact parameters. The position of the discontinuity in r_{min} is therefore inversely proportional to the ion energy.

Some modification to the scattering angle calculation is introduced at this point as numerically integrating equation (5.5) is awkward at impact parameters approaching r_{min}, since the integrand (5.6) becomes infinite at this point. In order to remove the singularity at r_{min} and make the region of integration finite a change of variables is introduced

$$\cos x = \frac{r_{\min}}{r}. \tag{5.7}$$

Equation (5.5) can then be re-written as

$$\theta(\varepsilon_0, b) = \pi - 2\int_0^{\pi/2} \frac{dx}{\sqrt{1 + F(x)}}, \tag{5.8}$$

where $F(x) = \dfrac{1}{b^2 \sin^2 x}\left({r_{\min}}^2 - b^2 - {r_{\min}}^2 \dfrac{V\left(\frac{r_{\min}}{\cos x}\right)}{\varepsilon_o} \right)$.

For equation (5.8) to be integrable at r_{min}, $F(x)$ needs to be finite as $x \longrightarrow 0$. To test whether this is true first consider the behaviour of V as $x \longrightarrow 0$. At small values of x

$$\frac{r_{min}}{\cos x} \approx r_{min}\left(1 + \frac{x^2}{2}\right), \tag{5.9}$$

and therefore the potential at small x can be approximated using

$$V\left(\frac{r_{\min}}{\cos x}\right) \approx V(r_{\min}) + \frac{x^2}{2} r_{\min}\left(\frac{\partial V}{\partial r}\right)_{r_{\min}}. \tag{5.10}$$

At $x = 0$ $r = r_{min}$ and so equation (5.6) can be re-written as

$${r_{\min}}^2 - b^2 - {r_{\min}}^2 \frac{V(r_{\min})}{\varepsilon_o} = 0. \tag{5.11}$$

Substituting (5.10) and (5.11) into the equation for F yields the result that for small x

$$F(x) = \frac{x^2}{\sin^2 x} \frac{r_{min}^{\ 3}}{2\varepsilon_o b^2} \left(\frac{\partial V}{\partial r} \right)_{r_{min}} . \qquad (5.12)$$

Since $\frac{\sin^2 x}{x^2} \rightarrow 1$ as $x \rightarrow 0$, $F(x)$ will be finite provided that the gradient of the potential is finite at the distance of closest approach, which will be true for all impact parameters which are larger than the repulsive core of the potential.

Finally (5.8) is re-arranged to make the difference implicit, which should reduce the incidence of numerical errors for small values of θ:

$$\theta(\varepsilon_o, b) = 2 \int_0^{\frac{\pi}{2}} dx - \frac{dx}{\sqrt{1 + F(x)}},$$

$$= 2 \int_0^{\frac{\pi}{2}} \frac{F(x)\, dx}{1 + F(x) + \sqrt{1 + F(x)}} . \qquad (5.13)$$

Figure 5.4(a) is a three-dimensional plot of the scattering angle as a function of energy and impact parameter. At large impact parameters most of the surface is flat and has a value close to zero: this clearly shows that for most parameters the scattering angle is very small and so the scattering will be highly anisotropic. This corroborates the experimental measurements of Vestal *et al* . However, there is a distinctive region at fairly small impact parameters where the scattering angle can reach large negative numbers, after which it slowly becomes positive, reaching a value of π at $b = 0$. This structure can be more clearly seen by looking at the individual energies plotted in Figure 5.4 (b). This clearly shows that there is a small range of impact parameters for which the scattering angle quite suddenly becomes extremely large – these are the same regions of impact parameter for which the discontinuity in the distance of closest approach graph occurs (in Figure 5.3). Note that this feature depends on energy as well as impact parameter – the position of the peak (negative) angle occurs at decreasing impact parameters for increasing energies. In other words, the ion and the neutral have

(a)

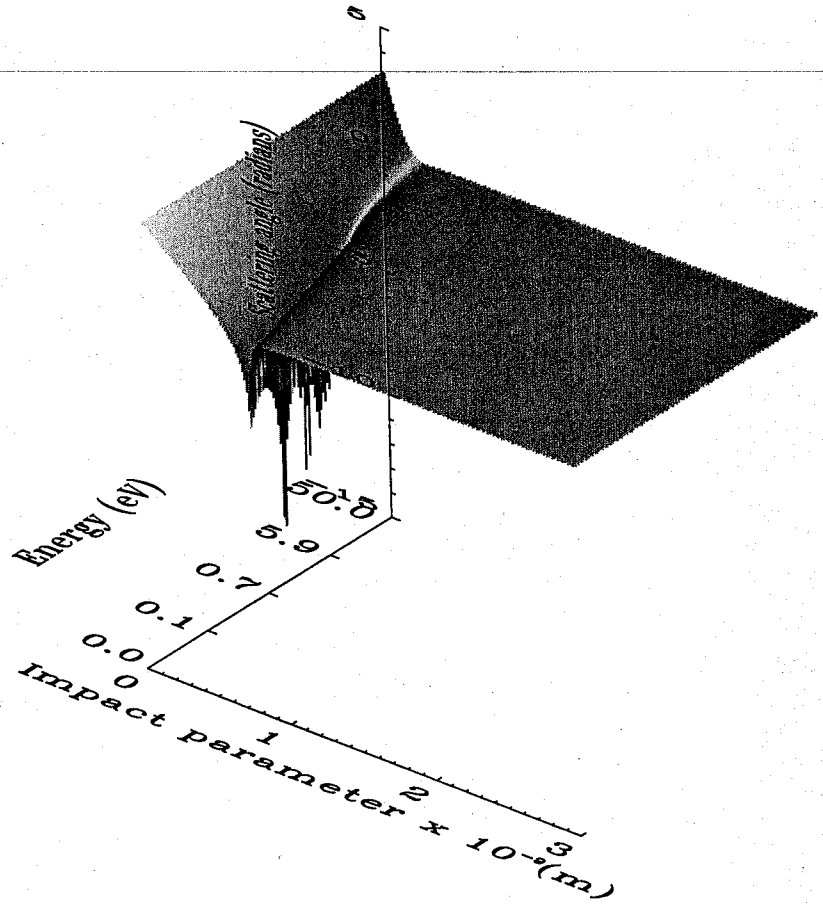

(b)

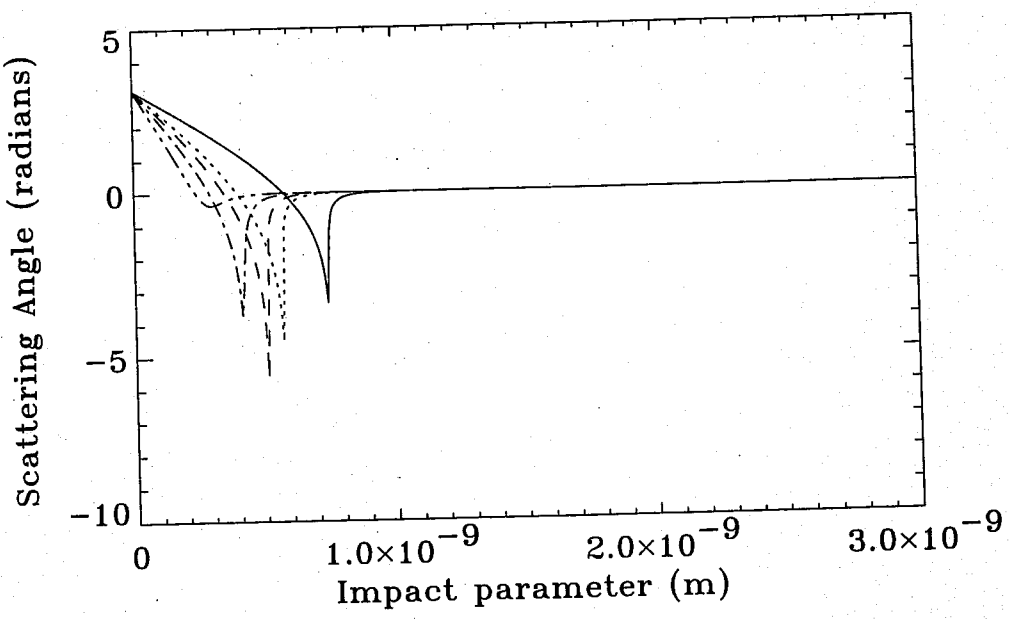

Figure 5.4 (a) Three dimensional plot of scattering angle as a function of impact parameter and centre-of-mass ion energy
(b) Scattering angle vs impact parameter for ion energies: 0.001eV (solid line), 0.2eV (dotted), 1.0eV (dashed), 10.0eV (dash-dot), 500.0eV (dash-three dots)

to approach more closely at large energies in order to scatter at large angles. The feature is very distinctive at low energies 0.001 – 1.0 eV (although the absolute magnitude has a large degree of scatter over this range) but decreases with energy, so that at 500 eV it has entirely disappeared. At very small impact parameters, the scattering angle becomes positive, increasing to a maximum scattering angle of π at $b = 0$. This sinusoidal scattering dependence is typical of hard-sphere collisions and represents scattering from the hard core of the potential.

Since the scattering angle is determined using classical considerations, an intuitive picture of the event can be built up by considering the interaction potential as a two dimensional surface along which the ion travels. This is represented schematically in Figure 5.5, with scattering shown for three different impact parameters. In case (a), where b is much larger than the radius of the potential well, the particle trajectory is relatively undisturbed, and the scattering angle is essentially 0. For case (b) where the impact parameter is of the order of the well radius, r_{well}, the particle enters the well and spirals toward the centre – the ion and neutral are trapped into orbiting one another as a "pseudo particle" before scattering, and a large scattering angle results. As b decreases the time spent in the well decreases and so does the scattering angle. Case (c) occurs

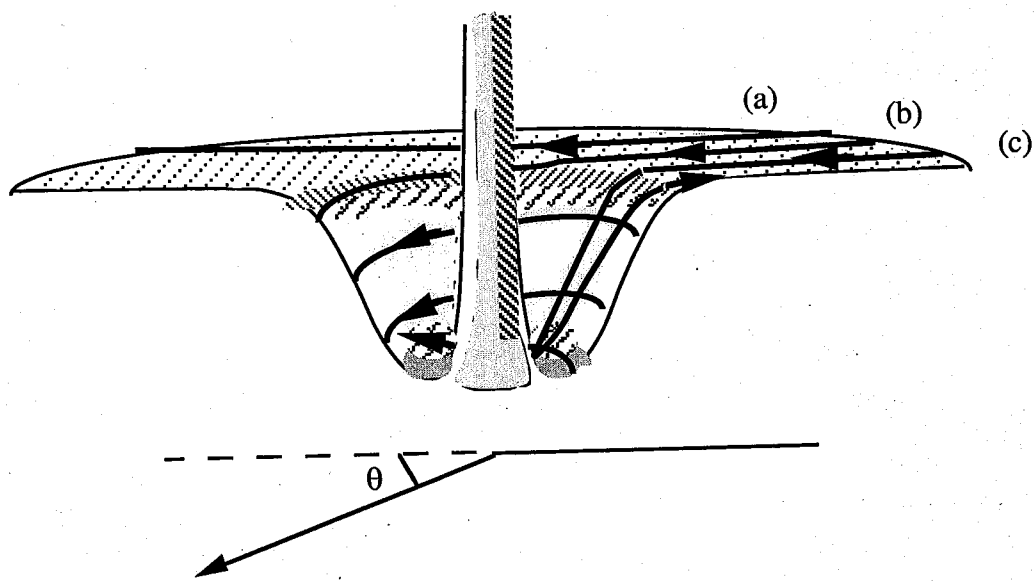

Figure 5.5 Schematic of an ion scattering in a 2D interaction potential, showing scattering behaviour for three different ranges of the impact parameter, b. **(a)** when $b >> r_{well}$, the radius of the potential well, the scattering angle, θ, is very small. **(b)** when $b \approx r_{well}$, orbiting occurs and θ is very large, **(c)** when $b \approx r_{core}$, the repulsive core of the potential, isotropic scattering occurs and $\theta \propto 2\cos^{-1} b$.

when b approaches r_{core}, the radius of the repulsive core potential. The interaction between ion and neutral is then similar to hard-sphere scattering and the scattering angle has a cosine dependence on b ($\cos\theta/2 \propto b$) so that as $b \rightarrow 0$ the scattering angle approaches π.

This particular picture is only valid for relatively low energy ions - say for the 0.001 - 1.0 eV range. As the ion energy increases the effect of the well potential has less and less effect on case (b) ions, since the impact parameter at which orbiting occurs decreases with increasing energy and so the likelihood of particle trapping also decreases. Therefore as the ion energy increases the position of the peak in the scattering angle becomes smaller; so that at very high energies ions experience only scattering corresponding to cases (a) and (c). This picture of the scattering explains the effects noted in Figure 5.4, and as well explains the dramatic drop in distance of closest approach at impact parameters corresponding to the well position (Figure 5.3). The sign of the scattering angle is determined by the form of equation (5.5) – the scattering angle is negative when the integral on the right hand side is $> \pi/2$, and positive when it is $< \pi/2$.

The unexpectedly large scattering angles for case (b) ions are known collectively as the rainbow angle, in analogy to critical angle scattering of light (see also Section 5.1.3). The impact parameter at which the rainbow angle occurs is inversely proportional to the ion energy, since higher energy ions need to be closer to the well minimum to be trapped, and very high energy ions will not be trapped at all. Hence the magnitude of the rainbow angle is proportional to the ratio of the ion energy and the maximum well depth.

5.1.3 Singularities in the scattering angle

There are several forms of singularity in the scattering angle, due to the form of the interaction potential, which have important physical effects on the scattering.

Orbiting

It is possible for the scattering angle, θ, to be greater than π, which means that the particle makes more than one revolution around the scattering centre. This phenomenon is known as orbiting. The conditions for this to take place can be determined by rewriting the numerator of (5.5) in terms of the classical angular momentum $J = M_r v_r b$. An effective potential, V_{eff}, for the relative radial motion can then be written as

$$V_{eff}(r) = V(r) + \frac{J^2}{2M_r r^2}, \qquad (5.14)$$

where $V(r)$ is the true interaction potential, J is the angular momentum, M_r is the reduced mass and r is the radial distance. The radial velocity can therefore be determined from

$$\frac{1}{2}M_r v_r^2 = \varepsilon_0 - Veff(r) \qquad (5.15)$$

where ε_o is the initial energy of the particle. If the radial velocity is small in the vicinity of the potential well minimum, and in particular if $\left(\frac{dV_{eff}}{dr}\right)_{r=r_{min}} = 0$ at r_{min}, then orbiting will occur.

Rainbow scattering

There is a singularity in the scattering angle which occurs for potentials with attractive minima, known as the rainbow effect, in analogy with the formation of rainbows by scattering of light at a critical angle. According to Mason and McDaniel ((1988), pg 151) this effect occurs at impact parameters for which the slope $\frac{d\theta}{db} = 0$, since the differential cross-section, σ, becomes infinite at this point:

$$\sigma(b,\theta) = \left|\frac{b}{\sin\theta}\frac{db}{d\theta}\right|, \qquad (5.16)$$

Effectively the scattering probability is large at this angle, but not infinite, since in the simulation the resolution is limited to the bin size for the impact parameter and in the "real world" the interaction potential is blurred by the effects of neighbouring particles.

Physically this corresponds to a range of energies and impact parameters which cause the particles to orbit each other as a pseudo-molecule before scattering. The magnitude of the rainbow angle varies inversely with the energy (see Section 5.3.1), so ions with energies of the order of a few eV will typically scatter at much larger angles than expected for small-angle elastic scattering. Since the rainbow angle has a large cross-section, and hence a large probability, it plays a major role in determining the transfer of energy into the perpendicular direction.

Glory scattering

This singularity occurs when the scattering angle $\theta \longrightarrow n\pi$, where n is an integer. Zero and even values of n represent forward scattering, odd values of n backward scattering. This effect is difficult to detect experimentally, since ions scattered in the forward direction are impossible to distinguish from the beam of unscattered ions, and ions scattered in the backward direction do not reach the detector.

The effect of these three singularities is shown schematically in Figure 5.6. Figure 5.6 (a) shows a general form the scattering angle as a function of impact

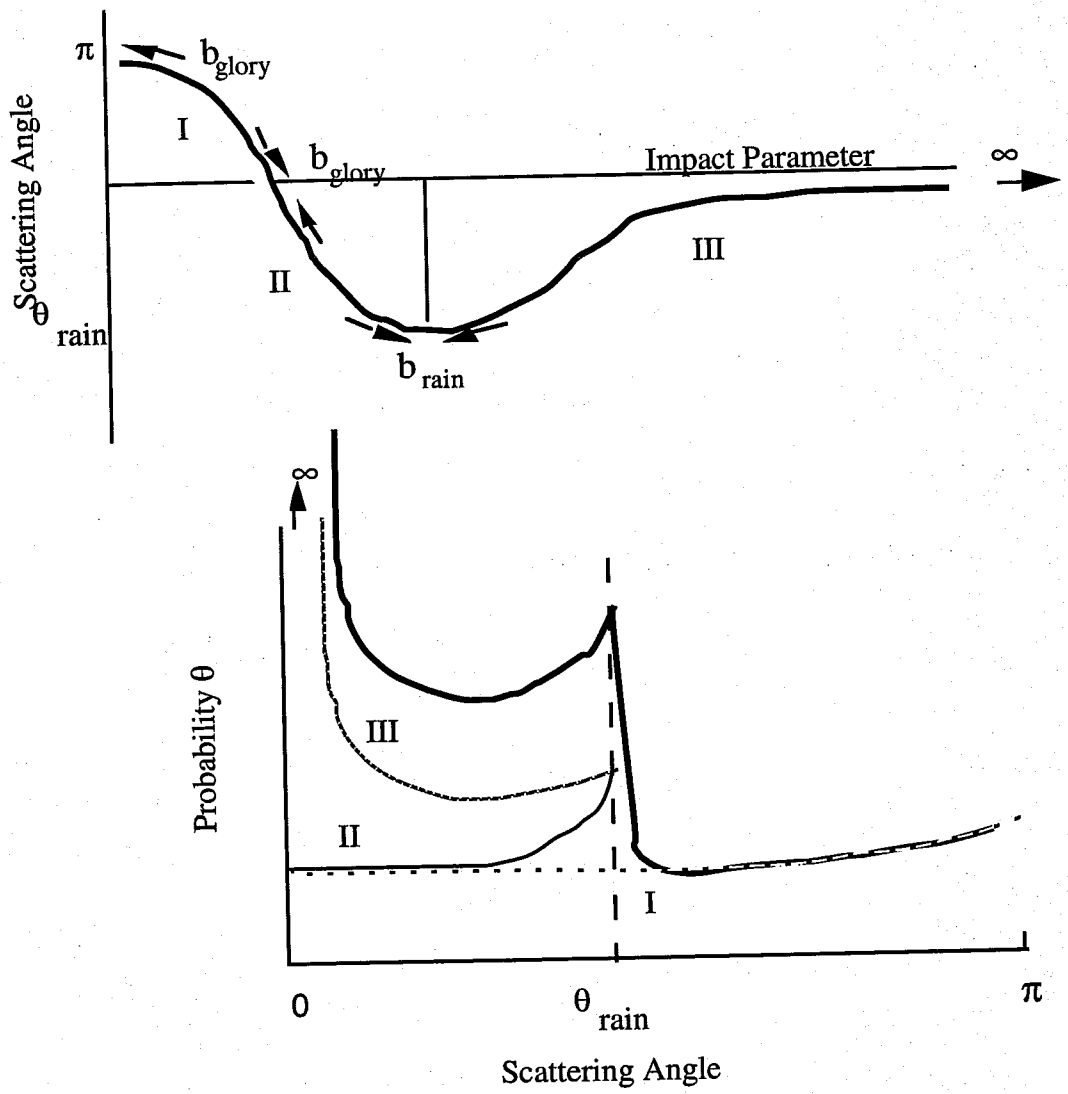

Figure 5.6 **(a)** The scattering angle as a function of the impact parameter for a given energy, showing the regions of impact parameters corresponding to glory and rainbow scattering **(b)** Scattering probability for the same energy, with the contribution from each region. The total probability, shown as a thick line, is the sum of I, II and III.

parameter at a given ion energy (c.f. simulation results in Figure 5.4 (b)). The scattering angle is divided into three regions which are bounded by impact parameters which correspond to glory scattering ($\theta = 0°$ or 180°) and rainbow scattering ($\theta = \theta_{rain}$). Figure 5.6 (b) presents the total scattering probability as a function of scattering angle, which is determined from the likelihood of scattering at a particular angle for each region, assuming that all values of b is equally likely. For example, in region III the scattering angle varies from very small at $b \rightarrow \infty$, to θ_{rain} at $b = b_{rain}$, and since there is much larger proportion of small scattering angles (over the impact parameter range) the probability curve peaks as $\theta \rightarrow 0$. There is also a small local peak at $\theta = \theta_{rain}$, since the curve $\theta\ (b)$ flattens out as $b \rightarrow b_{rain}$ and hence a relatively larger proportion of ions will be scattered at this angle.

These calculations determine θ for elastic scattering only. For collisions at small separations there is a high likelihood of charge exchange taking place – this is the phenomenon in which the neutral and the ion swap an electron during the collision (in fact the electron may be transferred several times, depending on the duration of the event). This results in a hot neutral atom and a thermal ion, and hence charge exchange has the effect of cooling ions accelerated in the sheath. In order to include charge exchange in the model, the charge exchange probability must be determined as a function of energy and impact parameter.

5.1.4 Charge Exchange

In a charge exchange collision an electron swaps from the neutral over to the ion. This makes a scattering angle of θ look like scattering at $\pi - \theta$, since the ion and the neutral have interchanged during the collision. Charge exchange is intrinsically a quantum effect and it cannot be obtained from the classical elastic scattering calculation, so it must be included empirically into the model using experimental values of the total charge exchange cross-section (the cross-sections are given in Appendix A). Each collision is then tested to determine whether charge exchange takes place and if the criteria are fulfilled then the scattering angle, θ, is swapped to $\pi - \theta$.

At a given energy, the probability of the collision involving a charge exchange interaction varies sinusoidally with impact parameter between 0 and 1, due to orbital resonances. At a critical impact parameter, which is dependent on energy, the probability decreases exponentially to zero (Rapp and Francis (1962)). This is shown schematically in Figure 5.7. For the purposes of the simulation, the charge exchange probability can be taken as $\frac{1}{2}$ for $b < a$ and as an exponential for $b \geq a$; with the maximum b for which a charge-exchange collision can occur chosen to be an arbitrary

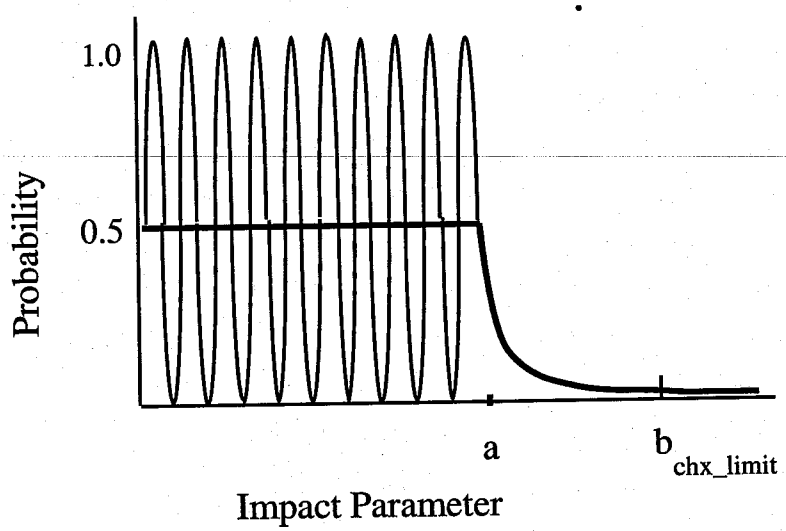

Figure 5.7 Variation of charge exchange probability with the impact parameter

limit, b_{chx_limit}. The function used to model this charge exchange probability is given by (Porteous (1993))

$$\Pr_{chx} = \frac{\sinh(b/a)}{2b/a}\left(\frac{6}{5+\cosh(b/a)}\right)^2 \qquad (5.17)$$

where b is the impact parameter, and a is the value at which the function starts to turn over. This function was chosen since it is flat at low impact parameters, decays as $e^{-b/a}$ for $b > a$ and is integrable. The turn-over point, a, is found using the total charge exchange cross-section, using

$$Q_{chx} = 2\pi\int_0^\infty P_{chx}\, bdb = 36a\pi\int_0^\infty \frac{\sinh(b/a)}{(5+\cosh(b/a))^2}db = 6\pi a^2 \qquad (5.18)$$

where Q_{ex} is the total charge exchange cross-section as a function of energy. An equation has been determined for Q_{ex}, using the expression (Mason and McDaniel (1988) pg 344)

$$Q_{chx}^{1/2} = a_1 - a_2 \ln \varepsilon \qquad (5.19)$$

where a_1 and a_2 are constants which depend on the gas type, and ε is the ion energy in eV. Fitting to experimentally measured cross-sections from Rapp and Francis (1962) gives values of $a_1 = 7.0$ and $a_2 = 0.38$.

The charge-exchange limit, b_{chx_limit}, is chosen to be $6a$, which effectively means that collisions with probabilities of $\leq 1\%$ are ignored. As this is an empirical, rather than a quantum mechanical description of charge exchange, the cross-sections derived using this method will not exhibit the peak structure due to orbital resonances which is typically associated with charge exchange, but they will have the correct shape and the right order of magnitude.

5.1.5 *Impact parameters*

In determining the scattering angle using equation (5.13) it is neither practical, nor possible, to integrate out to infinite impact parameters although the interaction potential has no limits in theory. Hence practical limits on b must be determined in order to integrate θ numerically. From Figure 5.4 it can be seen that at large impact parameters the scattering angle decreases very slowly toward 0. It is not necessary to include the infinitely small scattering angles at very large impact parameters, since these have almost no effect on the ion trajectory but take the same amount of computer time as a larger, more effective collision. At each energy, therefore, the impact parameter

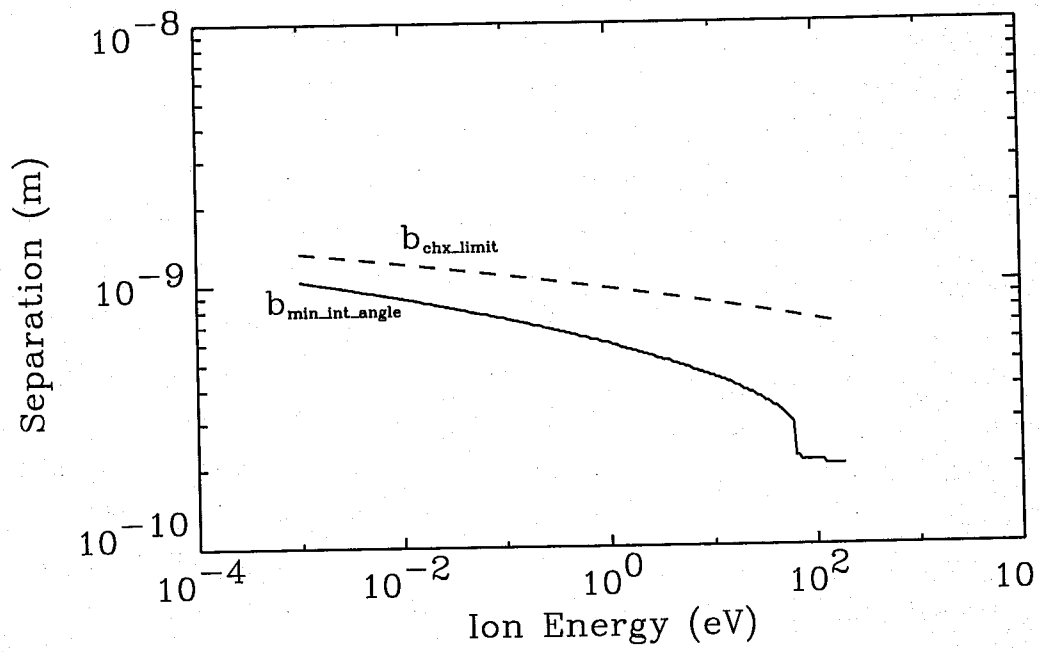

Figure 5.8 Limits on impact parameter used in the simulation, $b_{min\_int\_angle}$ corresponds to the minimum angle of interest and b_{chx_limit} is the maximum charge-exchange limit

corresponding to a scattering angle of 1°, $b_{min\_int\_angle}$, was chosen as an arbitrary cut-off for elastic collisions. However *all* charge exchange collisions (with impact parameters less than b_{chx_limit}) are included, since these *do* have a big effect on the ion velocity. Thus the limit of b at each energy is taken to be the maximum of $b_{min\_int\_angle}$ and b_{chx_limit}, and any event with an impact parameter larger than this is assumed to be a null collision. The limits are shown in Figure 5.8. It is found that b_{chx_limit} is larger than $b_{min\_int\_angle}$ for all the impact parameters of interest, and so b_{chx_limit} is chosen to be the maximum impact parameter used in determining the scattering angle.

5.2 Monte Carlo Code

The code models two parallel plates separated by a distance L, with a spatially uniform electric field, E, and a constant neutral gas pressure, p. Ions are injected at one electrode and accelerated in the field, making collisions with the neutral gas as they travel between the electrodes. The relative probability of an ion travelling at a given energy scattering at any angle between 0 and π is determined statistically from the ion collisions. Multiplying this "differential probability" by the correct scaling factor will give the differential cross-section – this scaling factor is difficult to calculate theoretically so it is determined from the experimental cross-section of Vestal *et al* . The relative forms of the simulation and experimental cross-sections are then compared. Various other measurements are made using the code, including the ion mobility, the division of energy between the parallel and perpendicular directions, and the angular distribution of the ions at the far electrode.

Although in general Monte Carlo codes will use distance- or time-of-flight techniques for generating ion paths, this simulation uses fixed time-steps which are much shorter than the mean free time between collisions. Although using fixed time-steps is a less efficient technique, the cross-section model is intended to be incorporated into a PIC plasma simulation and so must use methods which are compatible with the way particles are transported in the PIC code. At the end of each time-step an impact parameter, which is dependent on the relative energy of the ion, is chosen and this is used to determine whether the ion makes a collision. If a collision is found to occur then the energy and impact parameters are used as indices to look up the scattering angle from a predetermined table, and the new ion trajectory is calculated.

5.2.1 *Choosing an impact parameter*

In order to determine an impact parameter for the ion at each time-step a virtual cylinder is calculated from the ion trajectory. The length of the cylinder is determined by the distance traversed by the ion, and the radius is chosen so that the cylinder contains one neutral atom

$$r_{max} = \frac{1}{\sqrt{\pi L n_n}}, \tag{5.20}$$

where n_n is the neutral density, L is the length of the cylinder = $u_o\,\Delta t$, u_o is the ion velocity and Δt the time-step. Assuming that the neutrals have a spatially uniform distribution, the position of the neutral can be anywhere within the cylinder. The cumulative probability of the impact parameter having a certain value b is therefore

$$\Pr(b) = \frac{\int_0^b 2\pi L r\,dr}{\pi L r_{max}^2} = \frac{b^2}{r_{max}^2}. \tag{5.21}$$

Inverting this relationship, and using a random number , R, uniformly distributed between 0 and 1 to represent Pr(b), an impact parameter can then be chosen by

$$b = \sqrt{R}\ r_{max}\ . \tag{5.22}$$

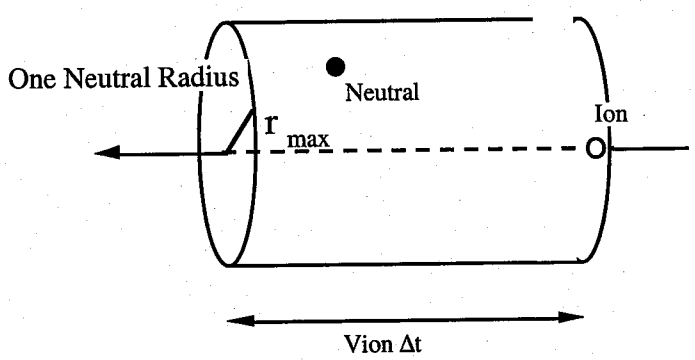

Figure 5.9 Virtual cylinder determined by the motion of the ion over one time-step - r_{max} is chosen so the cylinder contains one neutral.

5.2.2 *Centre-of-Mass Frame*

Once a collision has occurred, the new ion velocity must be calculated after scattering. The scattering angle is determined for the centre-of-mass (c-o-m) frame and so the pre-collision ion velocity must be converted to this coordinate system. The new velocity is calculated using the scattering angle in the centre-of-mass system, and then is converted back to the lab frame. This is shown schematically in Figure 5.10, where the dashed axes represent the c-o-m coordinate frame, v_{i_com} is the ion velocity relative to the c-o-m reference frame, θ is the scattering angle, ϕ is the azimuthal scattering, and α and β the angles of the c-o-m frame relative to the lab frame.

First a 3-D velocity distribution for the neutral is chosen by random sampling from a 300 K Maxwellian velocity distribution. The ion and neutral velocities in the lab frame are then given by

$$\tilde{v}_{ion} = \begin{pmatrix} v_{prl} \\ v_{prp} \\ 0 \end{pmatrix}, \qquad \tilde{u}_{neut} = \begin{pmatrix} u_{n\_x} \\ u_{n\_y} \\ u_{n\_z} \end{pmatrix}, \tag{5.23}$$

where v_{prl} is the parallel ion velocity, v_{prp} is the perpendicular velocity, and u_{n_x}, u_{n_y} and u_{n_z} are the components of the neutral velocity in the direction of the x, y and z axes respectively. Note that for this calculation the perpendicular ion energy is converted to velocity and assigned to the y-direction. This is purely for convenience, since once the new ion velocity is calculated the perpendicular component will be converted back to energy.

The centre-of-mass velocity is calculated using

$$\tilde{v}_{com} = \frac{1}{2}\left(\tilde{v}_{ion} + \tilde{u}_{neut}\right). \tag{5.24}$$

The ion velocity relative to the centre-of-mass frame is given by:

$$\tilde{v}_{ion\_com} = \tilde{v}_{ion} - \tilde{v}_{com} = \frac{1}{2}\begin{pmatrix} v_{prl} - u_{n\_x} \\ v_{prp} - u_{n\_y} \\ -u_{n\_z} \end{pmatrix} \tag{5.25}$$

The new x axis x' is determined from the direction of the centre-of-mass velocity, since this forms the axis of the collision. The y' and z' axes are chosen perpendicular to x' (see Figure 5.10). After scattering around x' by angle θ, the post-

collision trajectory is rotated by a random angle ϕ, uniformly distributed between 0 and 2π, to take into account the random orientation of θ around the collision axis. The new velocity in the centre-of-mass frame is

$$\tilde{v}'_{ion\_com} = \left|\tilde{v}_{ion\_com}\right| \begin{pmatrix} \cos\theta \\ \sin\theta\cos\phi \\ \sin\theta\cos\phi \end{pmatrix} \qquad (5.26)$$

The new ion velocity must then be converted back to the lab frame coordinate system. The relation between the centre-of-mass and lab axes is given by

$$\begin{aligned} x_{lab} &= \cos\alpha\cos\beta\, x' - \sin\alpha\cos\beta\, y' - \sin\beta\, z' \\ y_{lab} &= \sin\alpha\, x' - \sin\theta\cos\phi\, y' \\ z_{lab} &= \cos\alpha\cos\beta\, x' - \sin\alpha\cos\beta\, y' - \sin\beta\, z' \end{aligned} \qquad (5.27)$$

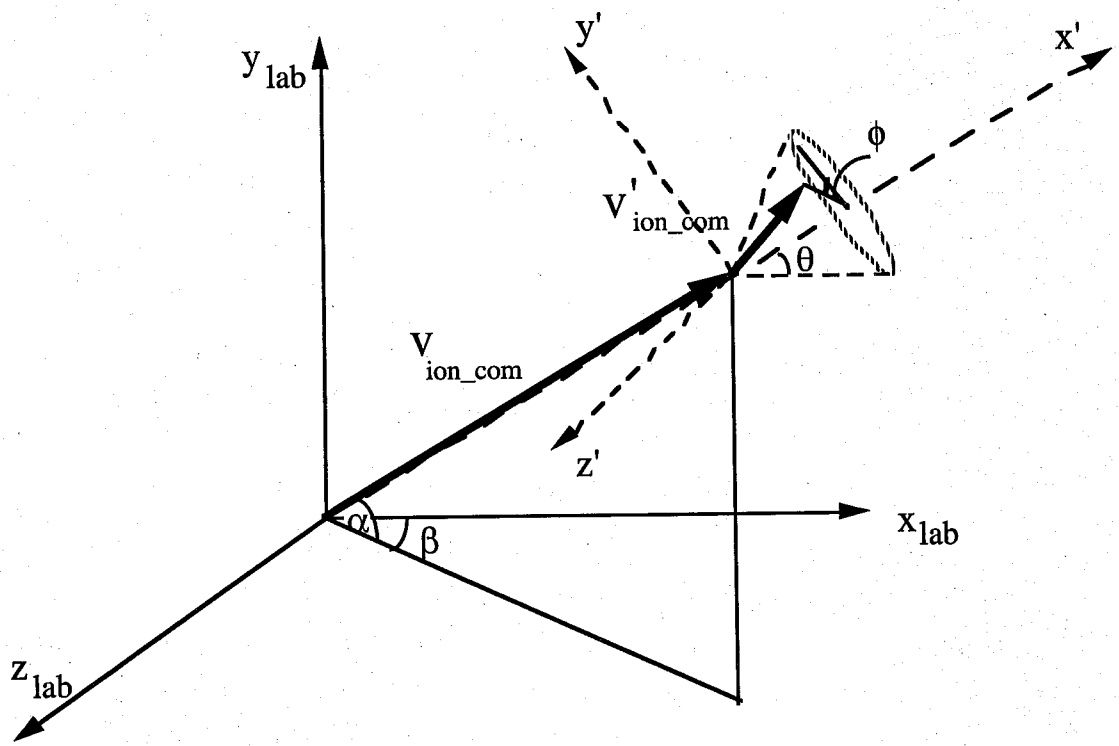

Figure 5.10 Diagram of the ion velocity after a collision with scattering angle θ; where v_{ion_com} is the ion velocity relative to the centre-of-mass frame frame (which is unchanged by the collision). (x_{lab}, y_{lab}, z_{lab}) are the lab coordinate axes, and (x', y', z') the c-o-m coordinate axes, the two coordinate systems are related by angles α and β.

where $\cos\alpha = \frac{\sqrt{v_{ion\_com\_x}^2 + v_{ion\_com\_z}^2}}{|\tilde{v}_{ion\_com}|}$, $\sin\alpha = \frac{v_{ion\_com\_y}}{|\tilde{v}_{ion\_com}|}$

$$\cos\beta = \frac{v_{ion\_com\_x}}{\sqrt{v_{ion\_com\_x}^2 + v_{ion\_com\_z}^2}}, \quad \sin\beta = \frac{v_{ion\_com\_z}}{\sqrt{v_{ion\_com\_x}^2 + v_{ion\_com\_z}^2}},$$

and $v_{ion\_com\_x}$ etc, refer to the x, y and z components of the ion c-o-m velocity. Converting the post-collision ion velocity back into the lab frame coordinate system

$$\tilde{v}'_{lab} = |v_{ion\_com}| \begin{pmatrix} \cos\theta\cos\alpha\cos\beta - \sin\theta\cos\phi\sin\alpha\cos\beta - \sin\theta\sin\phi\sin\beta \\ \cos\theta\sin\alpha + \sin\theta\cos\phi\cos\alpha \\ \cos\theta\cos\alpha\sin\beta - \sin\theta\cos\phi\sin\alpha\sin\beta - \sin\theta\sin\phi\cos\beta \end{pmatrix}. \quad (5.28)$$

To return the ion velocity in the lab frame, the centre-of-mass velocity must be added back to the ion velocity

$$\tilde{v}'_{ion} = \tilde{v}'_{lab} + \tilde{v}_{com}. \quad (5.29)$$

And finally the velocities in the y and z directions must be combined to give the new perpendicular ion velocity.

$$v_{prp}^2 = v_{ion\_y}^2 + v_{ion\_z}^2. \quad (5.30)$$

5.3 Comparison with experimental results

To determine the accuracy of the model, results from the Monte Carlo simulation have been compared to available experimental results. In Section 5.3.1 the magnitude of the rainbow angle, and its relation to the well depth in the interaction potential is discussed. In Section 5.3.2 the differential cross-sections (which are determined statistically from many scattering events) are scaled to fit the experimental cross-sections determined by Vestal *et al* (1989), allowing a comparison between the shape of the simulation and experimental cross-sections. Section 5.2.3 determines the total elastic cross-section as a function of energy and compares this to total experimental cross-sections. Drift velocities, obtained by running the simulation for many different conditions of electric field and background gas pressure, are compared to experimental drift tube data from Ellis *et al* (1976), and to simple theory developed in Section 5.3.4.

Finally in Section 5.3.5 results showing the energy division between parallel and perpendicular directions and the resulting angular distributions at the end electrode are presented, and the effect of the cross-section shape on the transfer of energy into the perpendicular direction is discussed.

5.3.1 Rainbow Angle

From theoretical considerations (Vestal *et al* (1978), Lorents *et al* (1973)) the product of the rainbow angle and the ion centre-of-mass energy should be a constant. That is, over a range of energies $\varepsilon.\theta_{rain} = C_o$, where C_o (known as the reduced rainbow angle) depends on the well depth and is unique for each ion-neutral pair. Vestal *et al* determine the rainbow angle in reduced coordinates to be 130 ± 2 eV° from their experimental measurements, and calculate a potential well depth of 1.4 eV. Lorents *et al* determine an experimental value for $\varepsilon.\theta_{rain}$ of 115 eV°, and calculate a theoretical value of 116 eV°, using a well depth of 1.25 eV. Experimental measurements of the well depth (quoted by Vestal *et al*) vary from 1.23 ± 0.02 eV to 1.33 ± 0.02 eV.

A well depth of 1.25 eV was used in the simulation. This gave a reduced rainbow angle of 127 eV° for most of the energy range from 0.001 eV to 100 eV (see Figure 5.11), which compares reasonably well to the experimental and theoretical

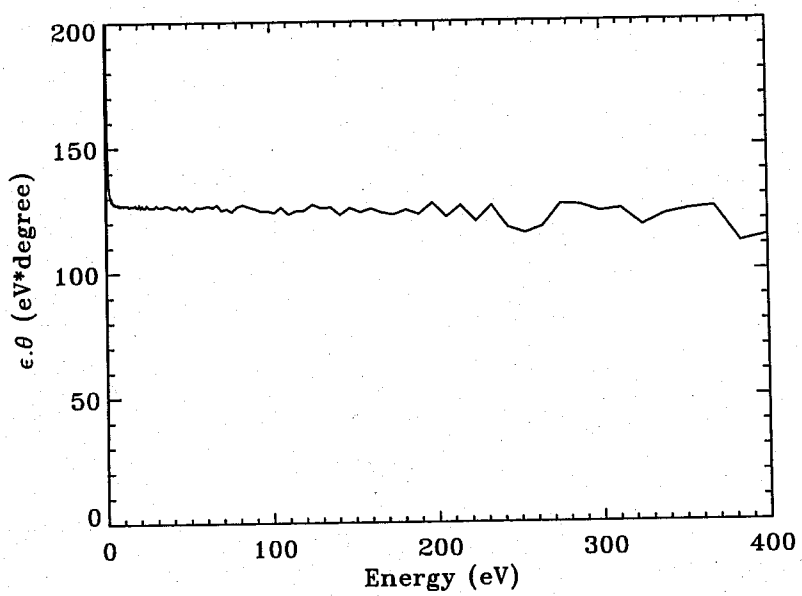

Figure 5.11 The product of the rainbow angle and the energy plotted as a function of energy, giving the relation $\varepsilon.\theta_{rain}$ = 127 eV°

results obtained by Lorents *et al* for the same well depth. At high energies the rainbow angle is less well defined, since it is inversely proportional to energy and at energies greater than ~100 eV it becomes difficult to differentiate from small angle scattering, leading to the numerical noise observed.

5.3.2 *Differential Probability of Scattering*

When the Monte Carlo code is run the scattering angles are stored as a function of energy for each collision to determine the differential probability of scattering. The probability is normalised at each energy, so the total probability of scattering, summed over all angles, is one. The differential probability is plotted as a function of energy and angle in Figure 5.12 (a), with the plot oriented so that energy decreases from front to back to clearly show the rainbow angle. At high energies the scattering probability is very anisotropic – with angles close to 0° and 180° – and clearly shows the symmetry in the probability for forward (elastic) and backward (charge exchange) scattering. For a collision at a given energy and impact parameter typically half of the ions will be forward scattered (i.e., scattered with angle θ) and half backward scattered (scattered with angle $\pi - \theta$). There is a break in the symmetry at low energies, as the probability of backward scattering goes to zero. Low energy ions tend to make glancing collisions with large impact parameters, which are very unlikely to involve charge-exchange. This can be clearly seen in Figure 5.12 (b) for energy 0.01 eV: there is a peak at small scattering angles but no corresponding peak close to π.

For intermediate energies – between about 0.5 and 10.0 eV – the rainbow angle is clearly visible as a sharp drop in the scattering probability. In Figure 5.12 (b), for energies 2 and 5 eV, it can be seen that the rainbow angle is actually a local peak. At this range of energies the probability of scattering at angles less than or equal to the rainbow angle is relatively large, with a local maximum at the rainbow angle. For angles greater than the rainbow angle the scattering probability is extremely small. Ions in this intermediate energy range can scatter at larger angles than is conventionally expected for forward scattering collisions, due to the effect of the rainbow angle. The rainbow angle becomes smaller with increasing ion energy, so the peak in the probability becomes indistinguishable from the small angle scattering peak at ion energies greater than 10 eV, and the scattering becomes strongly forward-peaked as is conventionally assumed.

The existence of the rainbow angle therefore means that ions in the energy range 0.5 - 10 eV have a greatly increased probability of scattering at angles larger than a few degrees, which can result in enhanced transfer of energy into the perpendicular

(a)

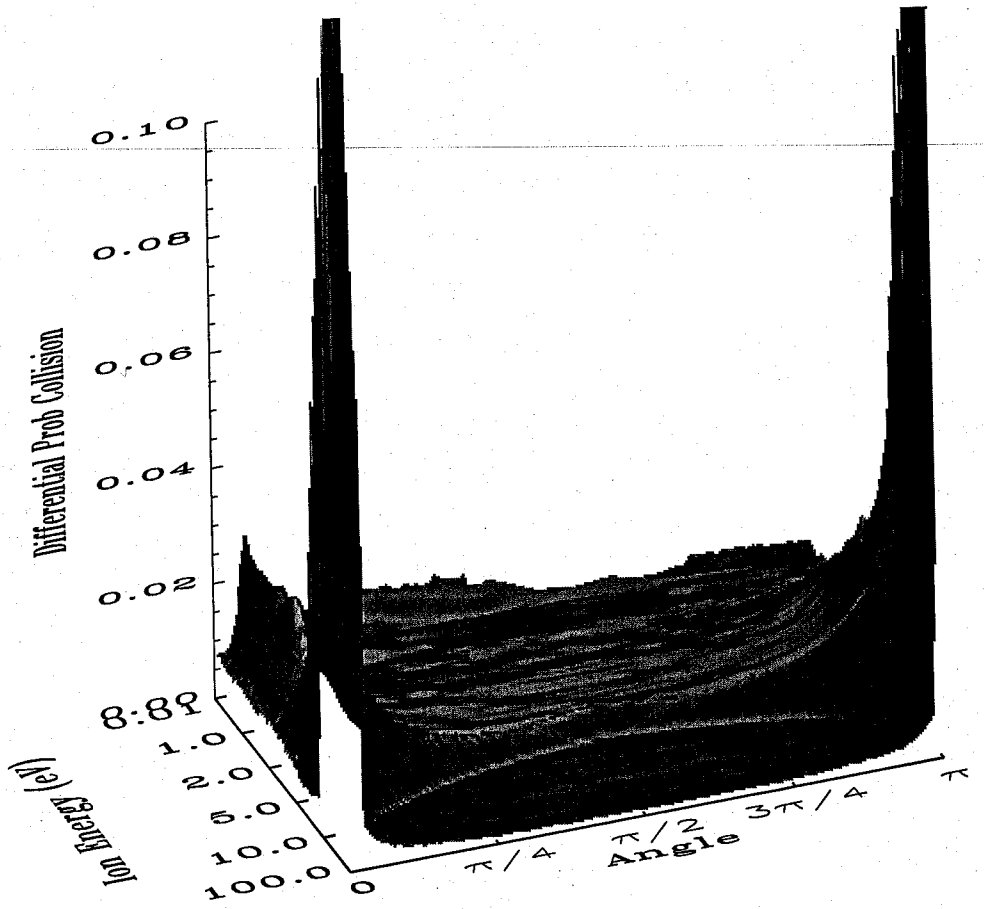

(b)

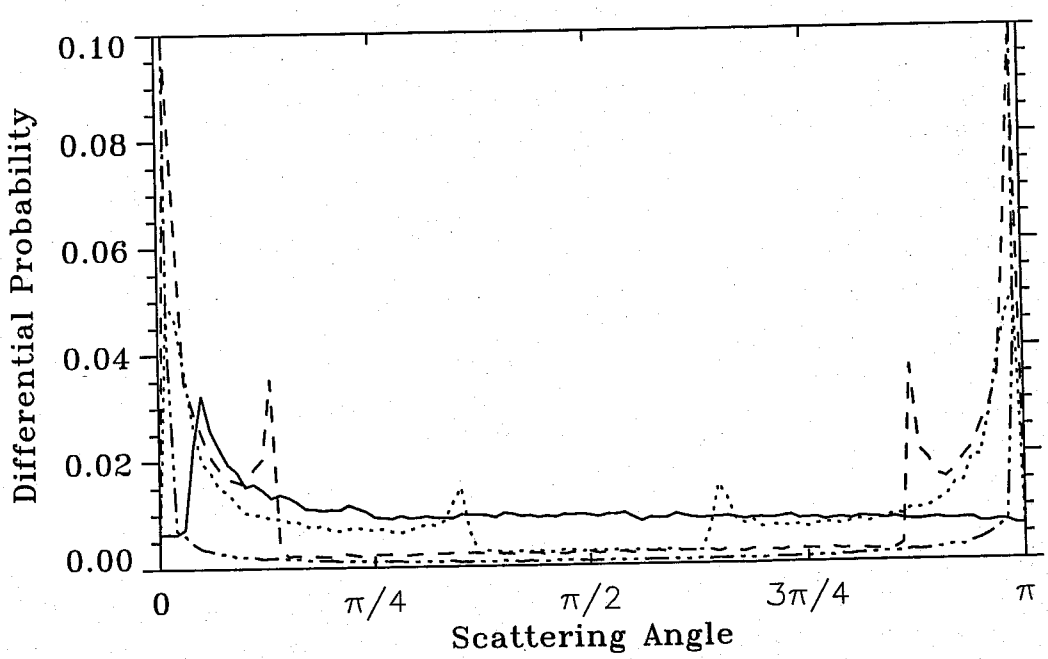

Figure 5.12 (a) Differential probability of collision plotted as a function of angle and ion energy
(b) Probability vs angle for ion energies:
0.01eV (solid line), 2.0eV (dotted), 5.0eV (dashed), 1000.0eV (dash−3dots)

direction. To determine the effect on the angular distribution at the electrodes consider an ion traversing the sheath of a low pressure rf plasma. Ions will tend to have at least one charge exchange collision in the sheath, since the average mean free path for charge exchange at a pressure of 20 mTorr is of the order of a few millimetres, while the maximum sheath width is typically 3 cm . After a charge exchange collision the ion energy will be low, and so there is an increased probability that the ion will make a second elastic collision with a large scattering angle. Ions which make multiple collisions in the sheath can therefore impact the electrode with substantially non-perpendicular trajectories.

Results of the differential probability of scattering are compared to the measurements of Vestal *et al* (1989) at discrete energies in Figure 5.13. Cross-sections derived from the simulation were all multiplied by a single scaling factor in order to compare to experimental results, since only relative values of the differential cross-section can be obtained. As can be seen the qualitative agreement between simulation and experimental results is very good, especially for the higher energies. The experimental measurements do not show the rainbow angle as clearly as the simulation, possibly because the measurements are limited by the experimental accuracy of the apparatus. In the experimental system also quantum interactions between the electron shells of the colliding ion and neutral lead to the ripples observed in the cross-section, which blur the shape of the cross-section. Quantum effects are not included in the simulation (Section 5.1.5) so the ripples are absent from the numerical cross-sections.

5.3.4 *Total Elastic Cross-section*

Assuming that most elastic collisions have scattering angles in the range 0 to $\pi/2$, integrating the differential cross-section from θ_{min} to $\pi/2$ will give the total elastic cross-section as a function of energy

$$q_{elas}(\varepsilon) = \int_{\theta_{min}}^{\frac{\pi}{2}} \sigma(\theta, \varepsilon) \sin(\theta)\, d\theta \qquad (5.31)$$

Integrating from $\pi/2$ to π just returns the fitted total charge exchange cross-section.

In order to determine the total elastic cross-section from the simulation it was found to be easier to substitute for the differential cross-section using $\sigma \sin\theta\, d\theta = b\, db$ from (5.16), since, as mentioned in the previous section, only relative values of the differential cross-sections are known. Equation 5.31 therefore becomes

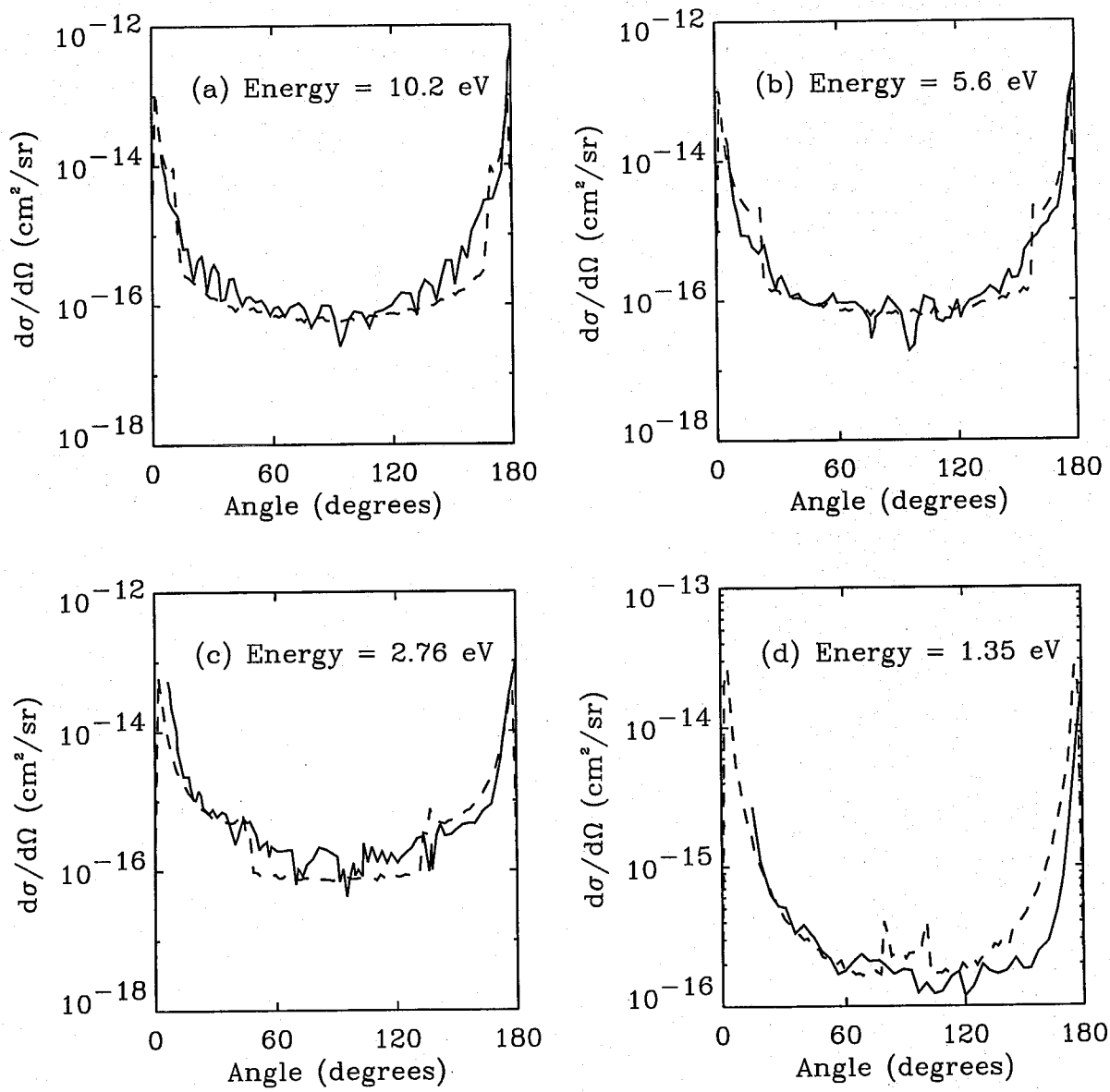

Figure 5.13 Comparison of simulation (solid line) and experimental (dashed line) results (from Vestal) for different centre-of-mass energies of the ion **(a)** 10.2 eV **(b)** 5.6 eV **(c)** 2.76 eV **(d)** 1.35 eV

$$q_{elas}(\varepsilon) = \int_0^{\infty} b\,db$$
$$= \frac{1}{2\pi}\int_0^{\infty} d(\pi b^2) \qquad (|\theta(b)| \geq \theta_{\min}) \tag{5.32}$$

However, limits for the integral in (5.32)) are not simple to calculate, since if conditions for a rainbow angle exist at a specified energy, then the scattering angle at this energy can be less than θ_{min} at three separate impact parameters due to the form of the dependence of θ on b. This is shown schematically in Figure 5.14. Instead it is easier to re-write (5.32) in terms of the impact parameter limits.

$$q_{elas}(\varepsilon) = \frac{1}{2\pi}\left[\int_0^{a_1} d(\pi b^2) + \int_{a_2}^{a_3} d(\pi b^2)\right]$$
$$= \frac{1}{2\pi}(a_1 - a_2 + a_3) \tag{5.33}$$

In general a_1 and a_2 are very close in value for most energies, even when the rainbow angle is present, and so a reasonable approximation is to simply use a_3 to determine the total cross-section. The total elastic cross-section calculated using equation (5.32) is plotted in Figure 5.15, together with the cross-section obtained by fitting to experimental values (see Appendix A) and discrete values obtained by integrating over the differential cross-section from Vestal *et al* . The first thing to note is

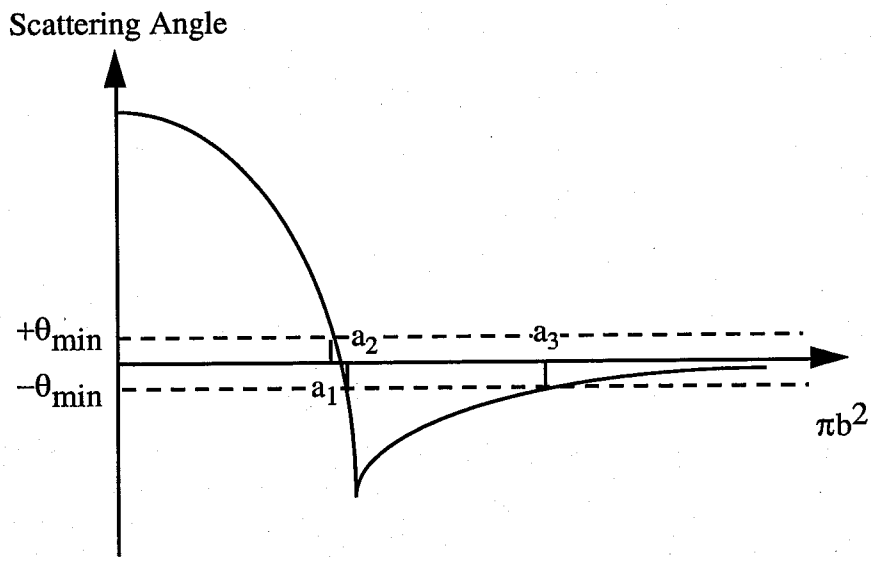

Figure 5.14 Schematic of scattering angle as a function of the impact "area", πb^2, showing the intercepts a_1, a_2 and a_3 at which $|\theta| < \theta_{min}$

the discontinuity in both the calculated cross-sections at an energy which is found to depend on the value used for θ_{min}. Looking at Figure 5.8 it can be seen there is a sudden drop in $b_{min\_int\_ang}$ at the same energy. This is due to the inverse proportionality of the rainbow angle to energy – at a critical energy the rainbow angle becomes less than θ_{min} and since the highest probability of scattering is for angles less than θ_{rain}, this causes a noticeable drop in the integrated cross-section. The energy of the discontinuity can be determined from

$$\varepsilon_{disc} = \frac{\varepsilon.\theta_{rainbow}}{\theta_{min}} = \frac{127\ eV^{\circ}}{\theta_{min}}$$

From Figure 5.15 the discontinuity occurs at a value of ~ 120 eV, which corresponds well to the minimum angle of 1° used in the simulation. The experimental cross-section does not have the same discontinuity, since experimental conditions generally limit measurements to scattering angles of 20° - 80°, and so the small angle peak is not actually included for any of the cross-section measurements. Hence it would be expected that for energies greater than ε_{disc}, the numerical cross-section should be

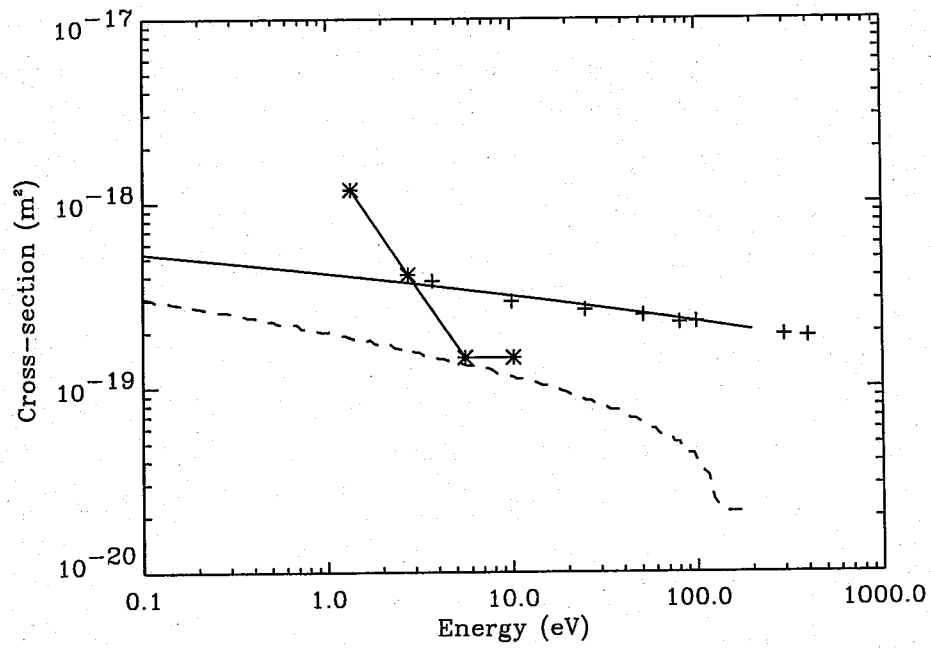

Figure 5.15 Total elastic scattering cross-section plotted as a function of energy, for the experimental fit (solid line with crosses), simulation (dashed line), and the integrated differential cross-sections in Vestal (asterisks)

equal to the experimental measurements, as neither include small angle scattering. Instead there is a factor of 5 difference between the results. Possibly this is due to errors in determining the absolute values of the experimental total cross-sections – differences of factors of 2 have been found between different experimental charge exchange cross-section measurements (Appendix A). The integrated differential cross-sections from Vestal *et al* , also plotted in Figure 5.15, have a very steep gradient at low energies, so although results at 5.6 eV and 10.2 eV agree well with the simulation cross-section, the value for 1.35 eV is almost an order of magnitude larger. This is possibly due to extrapolation of the results to zero degrees in order to integrate them.

5.3.5 *Comparison of simulation drift velocities with theoretical and experimental values*

The Monte Carlo code, having constant electric field and pressure, is essentially a model of a drift tube experiment. Drift velocity experiments have been performed since the early 1960's to study the behaviour of slow ions in gases and thus determine quantities such as the reaction rate coefficients and charge-exchange cross-sections (McDaniel 1988); and so there is a large body of experimental and theoretical results available for comparison to the simulation results.

The drift velocity of ions in a background gas of the same type is proportional to the ratio of electric field over pressure – as the field is increased ions can gain more energy in one mean free path, while increasing the pressure decreases the average distance between collisions. The parallel ion energy is primarily dependent on the charge exchange cross-section, as every charge exchange collision essentially drops the ion energy to zero, and is relatively insensitive to the elastic scattering cross-section, since scattering angles are small for ion energies greater than a few eV.

A simple theoretical model, derived in collaboration with Dr R. K. Porteous, is used to determine an analytic relationship between *E/p* and the drift velocity. The derivation assumes that the drift velocity is essentially determined by the mean free path for charge exchange and that elastic collisions have little effect. The mean free path between collisions can therefore be assumed to be constant for most conditions, as the charge-exchange cross-section is relatively invariant over the energy range 1-1000 eV (Mason and McDaniel (1988), pg 147). The derivation considers the temporal and spatial evolution of the ion energy distribution, considering the competing effects of collisions and acceleration in the electric field. At an initial position and time the ions are assumed to have an energy distribution *F(K)*, where $K = 1/2\,mv^2$. At a later time and position the distribution will have evolved to the form *F(K')*, where the change in

average energy of the distribution, due to acceleration in the field, is given by $\Delta K = eE\Delta x$. Since the mean free path, λ, is defined to be constant for each set of field conditions, the characteristic energy of the ions can be defined as $K_o = eE\lambda$. Particles which have collisions drop out of the distribution, so at the later time the distribution will have the form

$$F(K') = F(K)\, e^{\frac{\Delta x}{\lambda}} = F(K)\; e^{\frac{-\Delta K}{eE\lambda}} = F(K)e^{\frac{-\Delta K}{K_o}}. \qquad (5.34)$$

As $\Delta K \rightarrow 0$

$$F(K') = F(K+\Delta K) = F(K) + \frac{\delta F}{\delta K}\Delta K \qquad (5.35)$$

Equations (5.34) and (5.35) suggest that the energy distribution must be of the form

$$F(K) = F(0)e^{\frac{-K}{K_o}}. \qquad (5.36)$$

The energy distribution can be converted to a velocity distribution using $f(v)dv = F(K)dK/mv$, where m is the mass of the ion, and v is the velocity. The drift velocity is then obtained by integrating over the entire distribution

$$v_{drift} = \frac{\int_0^\infty v f(v)dv}{\int_0^\infty f(v)dv} = \frac{\int_0^\infty F(K)\frac{dK}{m}}{\int_0^\infty \sqrt{\frac{m}{2K}}F(K)\frac{dK}{m}}. \qquad (5.37)$$

Substituting for $F(K)$ in (5.37)and setting $x = \frac{K}{K_o}$ gives

$$v_{drift} = \sqrt{\frac{2K_o}{m}}\frac{\int_0^\infty e^{-x}dx}{\int_0^\infty \sqrt{x}\, e^{-x}dx},$$
$$= \sqrt{\frac{2K_o}{m\,\pi}}. \qquad (5.38)$$

The average drift energy of the ions, ε_d, is then given by

$$\varepsilon_d = \frac{1}{2}mv_{drift}^2 = \frac{K_o}{\pi} = \frac{eE\lambda}{\pi}. \qquad (5.39)$$

Re-arranging (5.39) and substituting $\lambda = \frac{1}{n_n Q_{exch}}$, where n_n is the neutral density and Q_{exch} is the charge exchange cross-section, gives the equation

$$\frac{E}{p} = \frac{\pi G}{e} \varepsilon_d Q_{exch}(\varepsilon_d) \qquad (5.40)$$

where p is the pressure, and G is Loschmidt's number = 3.2×10^{22} $m^{-3}Torr^{-1}$ (used to convert the pressure, in Torr, at 300K to the atomic number density). This has the same general form for E/p as given in Mason and McDaniel (1988, pg 149), but with an additional multiplying factor of $\pi/\sqrt{2}$. Mason and McDaniel derive their equation using kinetic techniques, assuming that ions make hard sphere collisions.

At low field conditions, v_{drift}, the drift velocity of the ions approaches the average thermal velocity of the neutrals, and so the random component introduced to the drift velocity through collisions with the neutrals becomes important to the distribution . A generalised form for the average ion energy, ε_{av}, must therefore include both the directed drift energy (due to the field) and the average neutral temperature, i.e., $\varepsilon_{av} = \varepsilon_d + kT_n$. Equation (5.40) must then be re-written as

$$\frac{E}{p} = \frac{\pi G}{e} \sqrt{\varepsilon_d \varepsilon_{av}} Q_{exch}\left(\sqrt{\varepsilon_d \varepsilon_{av}}\right) \qquad (5.41)$$

This equation includes the randomising effect of the neutrals at small drift energies, and reduces to (5.40) for high energies. If kT_n is constant for all conditions and the charge-exchange cross-section is only slowly varying with energy, then at high field conditions E/p will be proportional to the drift energy, and at low E/p to the square-root of the drift energy. The change in gradient is due to the importance of the neutral temperature at very low fields, since for these conditions the thermal velocity of the neutrals will be of the same order as the drift velocity.

The simulation results are plotted in Figure 5.16, together with experimental results of argon drift velocities determined from drift tube experiments by Ellis *et al* (1976), and calculations from the theory derived above, and quite outstanding agreement is found between the results from all three methods. The change in gradient in going from high field/low pressure conditions to low field/high pressure conditions can be seen very clearly. The solid lines are empirical fits to the theoretical results at low and high values of E/p, which show that $v_{drift} \propto E/p$ for $E/p < 10$ and $v_{drift} \propto (E/p)^{0.6}$ for $E/p > 10$. These relationships match well to the predictions given above, and agree with theoretical work by Mason and McDaniel (1988).

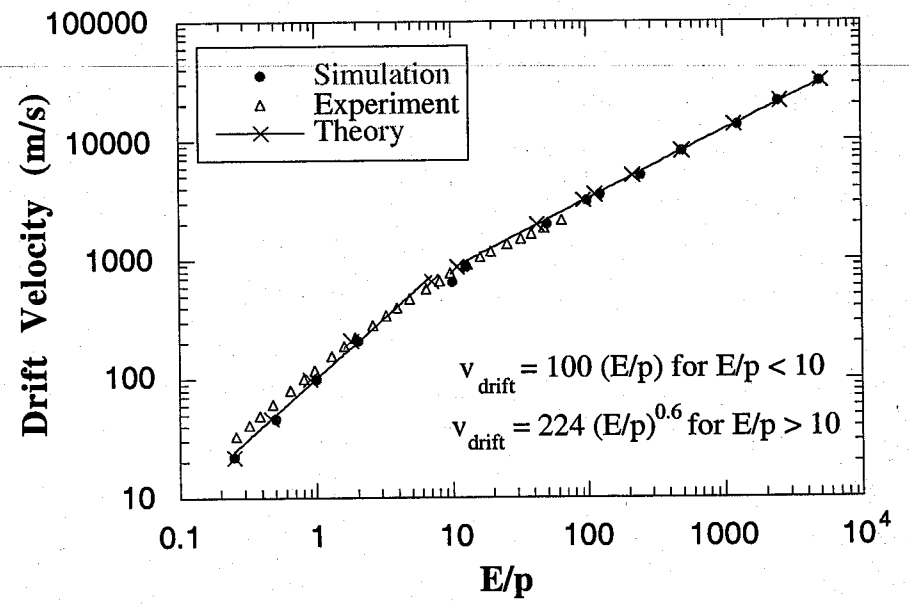

Figure 5.16 Drift velocity of argon as a function of *E/p* (in V m^{-1} $mTorr^{-1}$), showing experimental results (from Ellis *et al* 1976); numerical results from the simulation; and calculations from (5.42). Two fittings are shown for low and high values of *E/p*.

5.3.6 Average energy

As ions traverse the length of the drift tube they are accelerated by the electric field, and decelerated by collisions. When the energy as a function of position is determined for many ions (to obtain good statistics 10^6 or more ions are used in the Monte Carlo simulation) it is found that the average energy in both the parallel and perpendicular directions rapidly reaches a steady-state value within a few mean free-path lengths from the anode. The magnitude of this steady state value is determined by the ratio of electric field to gas pressure *E/p*, since the period of acceleration in the field is restricted to the mean free time between charge-exchange collisions, after which the ions lose most of the energy they have gained. The average total ion energy is therefore determined by the magnitude of the charge exchange cross-section.

In an elastic scattering event only a small fraction of the ion energy is lost through momentum transfer to the neutral, the rest is partitioned between the parallel and perpendicular ion energies, according to the angle of scattering. The relative proportions of energy in the parallel and perpendicular directions is therefore largely determined by the elastic cross-section. For most energies the scattering angles are

small and so most of the energy is stored in the parallel direction, however at very small values of E/p this can reverse.

From Figure 5.17 (a) the product of mean free path and pressure for both charge exchange and the total mean free path (which includes both charge exchange and elastic scattering) are plotted. At high E/p both exhibit the same power-law dependency on E/p, since for large ion energies the probability of charge exchange and elastic scattering collisions are approximately equal. Experimental measurements of the total energy also show this (Appendix A). At low E/p the mean free path for charge exchange decreases more rapidly since low energy ions are less likely to make charge exchange collisions.

In Figure 5.17(b) the steady-state values for parallel and perpendicular energies are plotted as a function of E/p. Both energies are found to have a power law dependence on E/p for values greater than the thermal energy. The parallel energy is found to be proportional to $(E/p)^{1.2}$. Hence the average parallel velocity is proportional to $(E/p)^{0.6}$ – the same dependence found for the drift velocity for $E/p > 10$ (see Figure 5.16) – since at high field conditions the drift velocity is large and primarily in the parallel direction. The power law dependence of the energies is lost for small E/p, since the ion energy is no longer independent of the neutral temperature. Instead, at very low values of E/p, the parallel energy is equal to the neutral thermal energy in one dimension, $\frac{1}{2} kT_n = 0.025$ eV. The perpendicular energy is twice this value, since it includes the two perpendicular directions. Hence at low E/p the ion energy distribution becomes isotropic.

In Figure 5.17 (c) the ratio of parallel to perpendicular energy of the ions is plotted as a function of E/p. For most of the range the ratio of the energies is almost constant and can be fitted with the relation $E_{prl}/E_{prp} \propto (E/p)^{0.5}$, although E_{prl}/E_{prp} appears to saturate at high and low field values. At low field values saturation occurs because the ion energy distribution is determined by the neutral temperature and becomes isotropic, but the reason for high field saturation is not well understood. It looks to be due to a relative increase in the perpendicular energy at high E/p, which could possibly be a result of the shape of the differential cross-section at high energies. Whether this effect is physical or introduced by assumptions in the derivation of the cross-section is uncertain at this stage.

The ratio of average energy in the parallel and perpendicular directions is expected to be highly dependent on the shape of the differential cross-section. To test this the interaction potential was altered to determine the effect on the parallel and perpendicular energy distributions. The average parallel energy was found to be relatively insensitive to the shape of the interaction potential. This is because for most E/p a large proportion of the energy goes into the parallel direction, and so the parallel

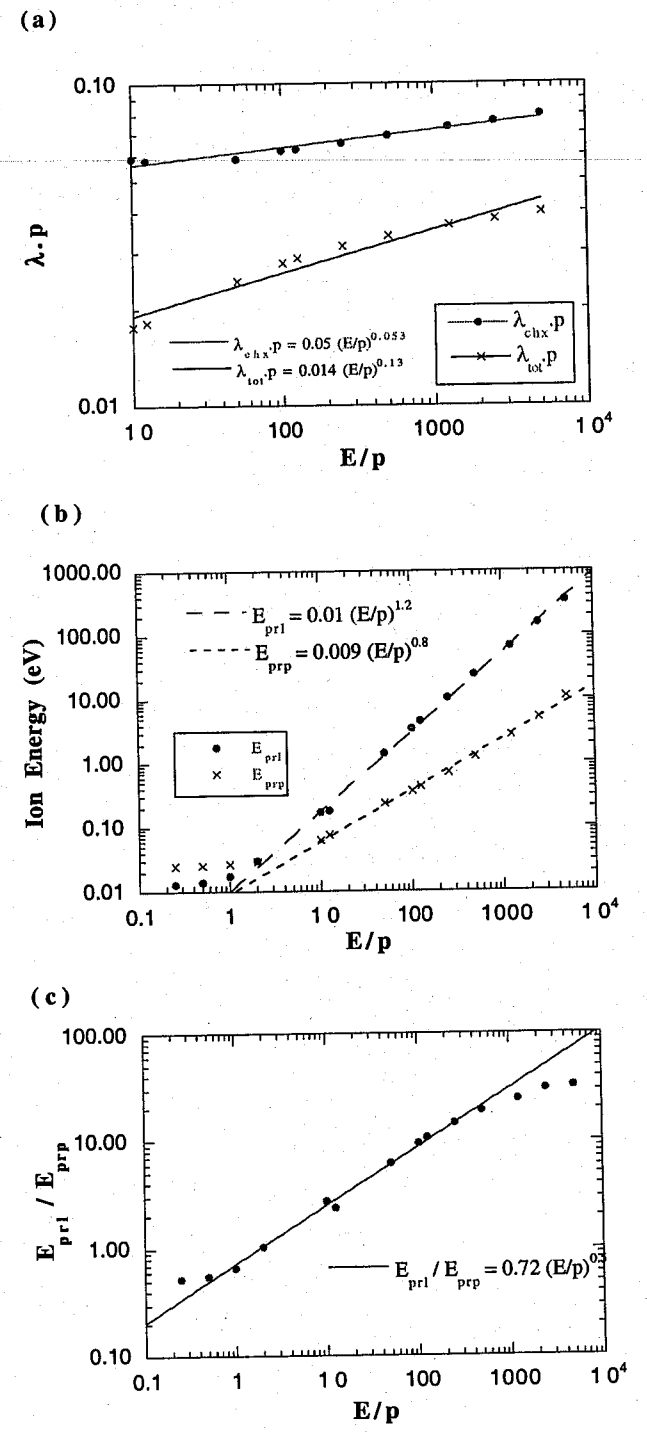

Figure 5.17 **(a)** The product of the mean free path and the pressure, for both charge exchange and total mean free paths, **(b)** The steady-state values of the parallel (dots) and the perpendicular (crosses) energies and **(c)** the ratio of parallel to perpendicular energy, all plotted as a function of *E/p*.

distribution is primarily determined by the rate of charge exchange collisions, which is relatively independent of small changes in the shape of the potential. The perpendicular energy, on the other hand, is strongly dependent on the width, depth and position of the potential well in the interaction potential, and any change in these parameters had a strong effect on the amount of energy transferred into the perpendicular direction.

5.4 Conclusion

This chapter details the development of angle- and energy-dependent cross-sections for Ar^+-Ar collisions. Classical collision techniques are used to determine elastic scattering due to the ion-neutral interaction potentials, and charge exchange is included empirically using fitted curves to experimental measurements of the total charge exchange cross-section.

The cross-section model was included in a dc Monte Carlo simulation and used to determine the relative differential cross-sections for comparison with experimental measurements by Vestal *et al* (1978); extremely close agreement was found between the two forms. Other measurements determined from the MC code, such as the reduced rainbow angle, the total elastic cross-section and the drift velocity as a function of *E/p*, are also compared to experiment, with excellent general agreement between the experimental results and simulation data. In particular the drift velocity results from the simulation showed quite remarkable agreement with both experimental measurements and with theoretical calculations outlined in this chapter.

The ion energy distribution in the parallel and perpendicular directions was also studied. For most of the range of *E/p*, the average energy parallel to the field was found to be dependent on the total charge exchange cross-section, while the average energy in the perpendicular direction was more a function of the elastic cross-section and heavily dependent on the form of the interaction potential.